Automated Mapping of K-feldspar by Electron Backscatter Diffraction and Application to $^{40}Ar/^{39}Ar$ Dating

Sandra McLaren[a]*, Steven M. Reddy[b]

[a] *Research School of Earth Sciences, Australian National University, Acton, Australian Capital Territory 0200, Australia.*

[b] *The Institute for Geoscience Research, Department of Applied Geology, Curtin University of Technology, GPO Box U1987, Perth, WA 6845, Australia.*

* corresponding author, present address*: School of Earth Sciences, University of Melbourne, Victoria, 3010, Australia.*

Tel.: +61 3 8344 7675,

Fax. +61 3 8344 7761

email: mclarens@unimelb.edu.au

Abstract

The ability to quantify feldspar microstructure using the electron backscatter diffraction (EBSD) method has direct application in the study of rock deformation and strain kinematics. However, automated EBSD analysis of low symmetry phases, such as feldspar, has previously proven difficult. Here, we successfully apply the EBSD method to a number of granitic feldspars and develop automated phase and orientation mapping to discriminate K-feldspar and plagioclase, and quantify orientation variations within individual K-feldspar grains. These results represent the first automated quantitative mapping of orientation microstructure in K-feldspar. We use the method to evaluate the relationship between microstructure and $^{40}Ar/^{39}Ar$ age, a controversial problem in thermochronology. In a granitic K-feldspar from central Australia, the range of observed orientation domains matches the small-intermediate and largest domain sizes predicted from multiple-diffusion domain modelling. *In situ* ultra-violet laser microprobe analyses show that the youngest ages from the $^{40}Ar/^{39}Ar$ age spectra are recorded by grain mosaic K-feldspars with diameter around 10-50 μm. These K-feldspars are the smallest coherent microstructural features observed on scales of > 1 μm. Large 250-1000 μm diameter microstructurally simple grains record the oldest ages observed in the age spectrum. These results suggest a first order relationship between K-feldspar microstructure and $^{40}Ar/^{39}Ar$ age and demonstrate a microstructural control on multidomain diffusion.

KEYWORDS: Electron Backscatter diffraction (EBSD); microstructure; deformation; thermochronology, argon, Multi-domain diffusion (MDD)

1. Introduction

Electron backscatter diffraction (EBSD) is a scanning electron microscope (SEM) technique that allows phase identification and the quantitative analysis of orientation variations in crystalline materials. The method utilises diffraction of electrons by the crystalline lattice, which generates a number of bands ("Kikuchi" bands) that each correspond to a set of lattice planes with a width that is directly related to lattice spacing (Randle, 2000). Together these bands form an electron backscatter diffraction pattern (EBSP) that is characteristic of both the phase and orientation of the crystal (e.g., Prior et al., 1999). By automatically collecting EBSPs over a predefined grid, EBSD data can be used to generate maps of phase and orientation data that allow the linkage of EBSD data to spatial position on a particular surface within the sample. Such an approach is performed on specially polished material surfaces and is non-destructive, allowing additional analytical techniques to be applied to the same sample. This approach therefore has certain advantages over much higher spatial resolution transmission electron microscopy (TEM) for investigating the relationship between microstructure and geochemistry. Unlike transmission electron microscopy, EBSD analysis can also be coupled directly with orientation contrast imaging (Prior et al., 1996), providing constraints on the microstructural context.

EBSD analysis of high symmetry geological materials such as olivine (Faul and Fitz Gerald, 1999), garnet (Prior et al., 2002), calcite (Bestmann and Prior, 2003), galena (Skrotzki et al., 2000) and zircon (Reddy et al., 2007) has yielded useful insights into the microstructural behaviour of these minerals during recrystallization, deformation and/or grain growth. However, EBSD analysis of lower symmetry phases, and particularly feldspars, has proven difficult. The reasons for this difficulty are the complex nature of feldspar EBSPs, the similarity of EBSPs between different feldspar phases, the various feldspar twin laws, pseudosymmetry in feldspars and problems associated with sample preparation. As a result automated EBSD analysis of feldspar has been difficult and the successful application of EBSD to feldspar (e.g. Prior and Wheeler, 1999; Jiang et al., 2000) has relied upon manual indexing of EBSPs, which is

time consuming and does not readily permit the integration of geochemical data within a spatially-constrained microstructural context afforded by automated EBSD mapping.

Here, we develop the use of automated EBSD mapping of alkali-feldspar in a variety of granitic rocks. We present a description of the method, operating conditions and indexing parameters employed. We then show the results of the automated EBSD mapping, including (1) the successful discrimination of alkali-feldspar and co-existing plagioclase and (2) the collection and analysis of quantitative crystallographic orientation data for K-feldspars.

We apply the EBSD method to the problem of linking quantitative orientation microstructure and $^{40}Ar/^{39}Ar$ age in K-feldspars. The mineralogy of K-feldspar has been extensively studied and its use in thermometry (e.g. Elkins and Grove, 1990) and argon geochronology (e.g. Spell et al., 1996; Swisher et al., 1993; McDougall, 1985) is well established. However, the thermochronologic use of K-feldspar remains controversial. The multiple-diffusion-domain (MDD) model (Lovera et al., 1989; Richter at al., 1991) attests that argon loss in K-feldspars is controlled only by thermally-activated volume diffusion and that the strong $^{40}Ar/^{39}Ar$ age gradients often seen in K-feldspars are the result of variable argon retention by diffusion domains of different sizes (Lovera et al., 1989; 1991). The notion of a number of different sized diffusion domains comes largely from the characteristic non-linear Arrhenius behaviour (Lovera et al. 1989). Individual diffusion domains are non-interacting and of simple geometry, and argon is lost instantaneously from domain boundaries. The fundamental tenet of the model is that the retention of argon during cooling in nature and the loss of argon during step-heating in the laboratory are controlled only by thermally-activated volume diffusion. The presence of a range of diffusion domain sizes yields a range in closure temperature that can be inverted to yield continuous cooling histories (Richter et al., 1991). As such, the method has become a potentially powerful tool in the reconstruction of exhumation histories and in the solution of various tectonic and structural geology problems (e.g. Dunlap and Fossen, 1998; McLaren et al. 2002) where it appears to give geologically reasonable cooling histories that are internally consistent and that are also consistent with apparent ages from higher and lower temperature chronometers, such as $^{40}Ar/^{39}Ar$ muscovite ages and apatite fission track ages.

However, only about half of all the K-feldspars analysed are suitable for thermal history analysis (Lovera et al., 2002) and there is considerable controversy regarding the validity of the method. In particular: (1) Lee (1995) questioned the assumption that volume diffusion is the only mechanism of argon loss, arguing that fast-pathway diffusion can also influence the argon release; comparisons of UV laserprobe Argon data with qualitative analysis of deformation microstructure support this (Reddy et al., 2001); (2) Parsons et al. (1999) questioned the presence of a discrete domain structure with the specific characteristics required by the MDD model as well as the assertion that K-feldspar microstructures form only at temperatures above the closure temperature of diffusive argon loss; and (3) the role of sub-micron features such as micropores, sub-grain boundaries and 'nanotunnels' remains unresolved (Fitz Gerald et al., 2006).

Central to all of these arguments is the question of how microstructure and argon loss are linked and to some extent this controversy reflects the inconsistency between the complex microstructural characteristics observed in K-feldspar and the relative simplicity of the MDD model. The work of Reddy et al. (2001) indicates that the way in which strain is accommodated within K-feldspar is a key control on the way in which the distribution of argon is modified. However, despite more than 20 years of work characterizing textural variations in K-feldspar, particularly at the sub-micron scale, there is still no explanation for the correlation between argon age and deformation-related microstructure reported by Reddy et al. (1999, 2001) other than the observation that orientation domain boundaries facilitate the grain-scale redistribution of argon. To help resolve this problem it is essential to integrate quantitative analysis of intragrain orientation variations with thermochronologic data. We link orientation microstructure and $^{40}Ar/^{39}Ar$ age by analysing the K-feldspar from a given sample using both $^{40}Ar/^{39}Ar$ step-heating (on separated K-feldspar grains) and *in situ* $^{40}Ar/^{39}Ar$ analysis (on individual K-feldspars in thin section). As such, this study builds on previous work investigating deformation-related sub-grains and Ar isotope systematics (Reddy et al., 1999; 2001) by providing the first link between *quantitative* orientation data, derived by EBSD, and $^{40}Ar/^{39}Ar$ ages.

2. Sample descriptions

Alkali-feldspar from three granitic sample suites was selected for this study. In all cases, macroscopically undeformed feldspars from undeformed granites were analysed to better enable results to be directly linked to samples typically used in the MDD approach. Compositionally, the analysed feldspars range from grains which are obviously perthitic under the light microscope, to homogenous microcline or orthoclase grains.

2.1 Big Lake Suite Granites, Warburton Basin, Australia

The Big Lake Suite granites are of Carboniferous age (323 ± 5 Ma and 298 ± 4 Ma; Gatehouse et al. 1995), and intrude the Warburton Basin at the base of the Cooper/Eromanga Basin in northern South Australia. The granites are compositionally and texturally complex and three samples exhibiting a variety of textural characteristics were chosen. These samples were obtained from core material extracted from three petroleum exploration wells; Sample 02-149 from a depth of 2895.2 metres in Moomba-1; Sample 01-147 from a depth of 3056.7 metres in Big Lake-1 and 02-152 from a depth of 3748.8 metres in McLeod-1. Uncorrected temperatures in the granite range from 160-230°C, and at least in part represent a recent increase in geothermal gradient associated with high-temperature fluid-flow (McLaren and Dunlap, 2006). Sample 02-149, containing K-feldspar, plagioclase, quartz and biotite, is the most pristine of the three samples. In hand specimen it is characterized by classic igneous textures and highly lustrous euhedral crystal faces. Individual alkali-feldspar grains are coarsely perthitic, show good crystal shape, and an almost total absence of alteration features such as clay minerals or dissolution pits (McLaren and Dunlap, 2006). Sample 02-147 shows complex textural features on the scale of individual grains and also complex grain boundary zones; the feldspars are characterized by moderate development of 10-50 μm clay mineral laths and perthitic exsolution textures. In hand specimen the sample is characterized by sugary-textured opaque feldspar. The third sample (02-152) exhibited extremely complex textural features with feldspar grains characterized by large overgrowths of highly altered mica and clay minerals, probably as a result of extensive

hydrothermal alteration and/or recrystallization. This sample ~~was unable to~~ be polished to sufficiently high quality for EBSD analysis to be performed.

The alkali-feldspars in all three samples are almost pure orthoclase containing only very minor amounts of Na (< 1.6 wt%) and Ca (< 0.04 wt%). The average of a number of point analyses give alkali-feldspar compositions in the range $An_{0-0.1}Ab_{4.3-8.2}Or_{91.7-95.7}$. (Table 1). Coexisting plagioclase in perthitic exsolution lamellae is almost pure albite with a composition around $An_{3.2}Ab_{95.5}Or_{1.3}$ (Table 1). The granites are inferred to have intruded during compression associated with the Alice Springs Orogeny (Sun 1997) and the thermal conditions associated with this event in the region suggest that the granites are likely to be intermediate temperature melts, with crystallization temperatures ~ 700-750°C (Sun, 1997; McLaren and Dunlap, 2006).

2.2 Areyonga Formation boulder clast, central Australia

Sample 01-524 is a granitic boulder clast from the Areyonga Formation in the Amadeus Basin, Central Australia. The Areyonga Formation is a Neoproterozoic (c. 720-660 Ma; Corsetti et al. 2006) diamictite conglomerate with calcareous and lithic sandstone interbeds all of glacial origin. The conglomeratic material is extremely poorly sorted and contains abundant sedimentary and basement-derived clasts. The sampled granitic boulder clast is spheroidal, ~ 40 cm in diameter, and exceptionally well preserved, containing abundant pink K-feldspar, quartz, plagioclase and biotite. In thin-section the sample is characterized by typical igneous textures and the K-feldspars show no evidence for hydrothermal alteration or recrystallization. Around half of the feldspar grains are characterized by perthitic exsolution on scales of < 1 μm to around 50 μm. The K-feldspar component is almost pure orthoclase with point analyses giving an average composition around $An_{0.1}Ab_{5.0}Or_{94.8}$ (Table 1). Coexisting plagioclase in exsolution lamellae is almost pure albite with point analyses giving a composition around $An_{3.8}Ab_{96.5}Or_{0.6}$ (Table 1). There is no evidence for deformation on the hand specimen or thin section scale.

2.3 *Dead Fox Granite, central Australia*

The Dead Fox Granite is late Palaeoproterozoic in age (Zircon $^{207}Pb/^{206}Pb$ age = 1785 ± 4 Ma; Page, 1996) found in limited, scattered outcrops between the Tanami and Arunta Inliers in Central Australia. In hand specimen the sample contains distinctive large grey feldspar phenocrysts ranging from several millimetres to around 2 cm in diameter. The granite appears undeformed in hand specimen and thin section. The granite is part of Group 3 in the tripartite division of Australian Proterozoic igneous rocks of Budd et al. (2001). Petrogenetic considerations (e.g. Wyborn et al. 1997) suggest that these rocks are the products of relatively high temperature melting around ~ 1000°C as a result of melt-producing amphibole breakdown reactions.

In thin section, K-feldspar is associated with myrmekitic quartz and plagioclase in two main populations – coherent single grains (~ 350-1000 μm across) and disrupted grain mosaics (~ 20-50 μm). The large single K-feldspar grains are often surrounded by moats of K-feldspar-quartz-plagioclase myrmekite while the grain mosaic K-feldspars are themselves part of the myrmekitic texture, usually occurring on the margins of larger single K-feldspar, plagioclase or quartz grains (Fig. 1). Although models for the formation of myrmekite remain controversial, in the absence of evidence for deformation a symplectic crystallization model rather than a deformation-induced "myrmekitization" mechanism (e.g. Hippertt and Valarelli, 1998) is inferred for the origin of the texture in the Dead Fox granite. That is, the myrmekitic texture is considered to be the product of auto-metamorphic reactions occurring at relatively high temperatures during crystallization of the granite (e.g. Castle and Lindsley, 1993).

The composition of the K-feldspars is in the range $An_{0.1}Ab_{11.2}Or_{88.7}$ (Table 1). Despite the relatively high Na content, the K-feldspars exhibit only very rare perthitic exsolution textures when viewed under the transmitted light microscope. Optical twinning is also rare and turbidity is variable (Fig. 1).

3. EBSD Analysis

Petrographic thick (300 μm) sections of the granitic samples were prepared to allow the possibility of later $^{40}Ar/^{39}Ar$ analysis using the ultra-violet laser microprobe. The sections were polished sequentially at different grades of abrasive down to 0.25 μm diamond paste, and subsequently prepared for EBSD analysis by chemical-mechanical polishing using a vibrating polyurethane lap and colloidal silica (o.o6μm in pH10 NaOH) polishing fluid. Atomic number contrast (ANC) imaging using a backscatter detector, orientation contrast imaging using a forescatter detector (Prior et al. 1996) and EBSD analysis were all performed using a Philips XL30 Scanning Electron Microscope in the Microstructural Analysis Facility at Curtin University. To preserve the quality of the EBSD patterns, samples were not carbon-coated. Instead, samples were surrounded by carbon tape to reduce charging. An accelerating voltage of 20 kV, a working distance of 20mm and sample tilt of 70° was used for all orientation contrast and EBSD analyses.

EBSD data were acquired and processed using Oxford Instruments/HKL CHANNEL5 software using the settings summarised in Table 2. Theoretical match units for a range of different feldspars were either derived from the HKL crystal files supplied with the EBSD system, the Mineralogical Society of America's Crystal Structure Database or utilising the crystallographic and crystallochemical data obtained from from the Mincryst database (Chichagov et al. 2001). Empirical testing of the different match units with the samples was undertaken to optimise the indexing process. This empirical testing, though less sophisticated than the approach of Reddy et al (2008), showed that the best indexing was obtained using monoclinic orthoclase (a = 0.8563 nm, b = 1.2963 nm, c = 0.7210, β = 116.1°) and monoclinic albite (a = 0.8274 nm, b = 1.2991 nm, c = 0.7144, β = 116.1°) structure data derived from Prince et al (1973) and Winter et al (1979), respectively.

For all data, the mean angular deviation (MAD) between the empirically obtained pattern and the theoretical solution was generally low (Table 2). MADs greater than 1.5 were rejected as poor quality fits at the indexing stage of data processing. Following standard EBSD procedures, all EBSD data were noise reduced using a "wildspike" correction to remove individual mis-indexed points and a four-

neighbor extrapolation to correct for some zero solutions (see Reddy et al. (2007) for details).

The EBSD data from each area were processed in different ways to produce a series of maps that show different aspects of the microstructure. Band contrast is a fundamental property of the EBSP that is obtained from the contrast identified in the Hough transform (Hough, 1962) used to recognize band edges in the EBSP and index to a theoretical feldspar diffraction pattern (or match unit). Band contrast is susceptible to variations in crystallographic orientation, structural integrity, crystal damage and surface topography and is therefore particularly useful for qualitatively delimiting sample microstructure independently of any data processing. Band contrast maps were therefore used as a background over which phase or orientation data were draped. Phase maps were produced by assigning a different color to each identified feldspar phase. Orientation maps were produced using a 'texture' component in which each pixel is colored for minimum misorientation relative to a user-defined reference orientation from a particular EBSP selected on the map.

Crystallographic orientation data were plotted using Channel 5 *Mambo* software using lower hemisphere, equal area projections. All data are reported with respect to an arbitrarily assigned X-Y coordinate framework for the sample surface. This permits intra sample orientation variations to be investigated and only precludes linkage of these variations to a field coordinate system (e.g. geographical coordinates).

4. Discrimination of K-feldspar and plagioclase using automatic mapping

The successful discrimination of K-feldspar and plagioclase by EBSD is essential if the crystallographic orientation variation within individual feldspars is to be accurately quantified. The EBSPs obtained from the K-feldspar host and the associated perthitic plagioclase are very similar (Fig. 2), showing crystallographic orientations that are consistent with the established crystallographic relationships between these phases. Despite this similarity, automatic EBSD mapping was able to effectively discriminate between K-feldspar and plagioclase (Figs. 3a,c; 4a,c; 5a,c) and shows that alkali-

feldspars from the Big Lake Suite granite and the Areyonga Formation show some degree of perthitic exsolution at scales of < 1 μm to *c.*40-50 μm (Fig. 3a, 4a, 5a). Two problems were encountered associated with phase mis-identification. The first resulted in plagioclase EBSPs from a single area being systematically indexed as K-feldspar and is likely the result of automatic band selection not recognising or using critical discriminating bands. The second arises from apparent misindexing of individual EBSPs within areas comprising only K-feldspar, as identified by ANC imaging. The resulting "checkerboard" pattern is a typical characteristic of misindexing of phases or pseudosymmetry relationships in individual phases. However, compositional information in K-feldspar rich areas indicates an abundance of <3 μm cryptoperthite areas. Since these are smaller than the grid spacing of EBSP collection, many of the isolated analyses of plagioclase may be real rather than representing compositional misindexing (Figs. 3,4). The apparent mis-indexing is therefore partly a function of mapping resolution.

5. Quantifying crystallographic orientations in K-feldspar

Macroscopically undeformed feldspar phenocrysts from undeformed granitic protoliths show considerable intragranular orientation variations. Individual grains of alkali-feldspar from a granitic boulder clast from the Areyonga Formation (Fig. 3) record internal variations up to 17° that are accommodated by the formation of discrete low-angle boundaries within the feldspar. These low-angle boundaries form traces oriented in two directions at approximately 45° to the arbitrarily defined sample X-Y axes (Fig. 3d). The interaction of these two directions results in orientation domains from the 10-100 μm scale. The first of the boundary directions correspond to lines approximately parallel to (100) (Fig. 3e), although the similarity to the trace of perthitic exsolution (Fig 3a) indicates that the plane is probably $(\bar{6}01)$, the plane of minimum strain between two different monoclinic feldspars (Williame and Brown, 1974). The second direction is coincident with lines of low band-contrast (Fig. 3b) that have traces approximately 90° to perthitic exsolution traces. The similarity of {100}, {010} and {001} within the grain indicate that these boundaries are not likely to represent twin planes. They could

represent {010} and {001} cleavage planes, but with no constraints on the 3 dimensional geometry of the boundaries this is not possible to verify.

Feldspars from the Big Lake Suite granite (Figs. 4, 5) record less orientation variations and do not show the discrete low-angle boundaries that characterise the Areyonga Formation sample. Instead the grains show gradual changes in orientation of *c.* 1°/100μm (Figs. 4d, 5d). Such variations are not consistent with common feldspar features such as twinning and cleavage and are interpreted to reflect the accumulation of dislocations within the feldspars. Since the samples are macroscopically undeformed, the strain accommodated by these dislocations is interpreted to represent the response of the feldspar to thermal stresses during subsolidus cooling.

6. Application to $^{40}Ar/^{39}Ar$ thermochronology

Previous studies have attempted to address the issue of argon diffusion in K-feldspars, and particularly the relationship between microstructure and $^{40}Ar/^{39}Ar$ ages. For example, Wartho et al. (1999) report a laser ablation microprobe study of the Benson Mines Orthoclase, a gem-quality K-feldspar characterized by very simple microstructure, and Fitz Gerald and Harrison (1993) report a detailed light microscopy and TEM study of K-feldspar MH-10, a sample well characterized by step-heating and MDD modelling. Only Reddy et al. (2001) have attempted to link $^{40}Ar/^{39}Ar$ ages directly to microstructural observations at a high spatial resolution by (1) determining $^{40}Ar/^{39}Ar$ ages on a single K-feldspar grain using both step-heating and a high spatial resolution ultra-violet laser microprobe, and (2) characterizing the deformation-related microstructures in the same grain using orientation contrast imaging. However, quantitative orientation data was not included in this previous work and the success of the EBSD method documented here has the potential to provide extra constraints on this problem.

Of the samples subject to EBSD analysis, only feldspar from the Dead Fox Granite was subject to detailed in-situ $^{40}Ar/^{39}Ar$ analysis. This sample was chosen on the basis of (1) its large range in recorded $^{40}Ar/^{39}Ar$ ages from ~ 700 Ma to ~1550 Ma,

and (2) its generally old ages (Fig. 6). Unfortunately, we are unable to link the microstructures identified in the other alkali-feldspar samples with their argon ages as the generally young ages of these grains (< 600 Ma) mean that we could not precisely resolve ages of individual orientation domains using existing analytical facilities.

6.1 Furnace $^{40}Ar/^{39}Ar$ step heating

The age spectrum of K-feldspar from the Dead Fox Granite is characterized by ages that increase, essentially monotonically, as temperature is raised (Fig. 6; Appendix). The first 20% of the gas release appears to be contaminated, as indicated by the large difference in the age of isothermal steps. This pattern is characteristic of excess argon associated with the decrepitation of Cl-rich fluid inclusions (Burgess et al., 1992, Harrison et al., 1994). The oldest age recorded in the age spectrum (1547 ± 33 Ma; Fig. 6) is ~ 200 Ma younger than the intrusion age of the granite. This suggests that the granite has experienced post-intrusion heating, probably during the regional 1590-1560 Ma Chewings Orogeny (e.g., Teyssier et al., 1988; Hand and Buick, 2001). However, the absence of evidence for deformation and/or recrystallization suggests that the granite did not experience any deformation or metamorphism during this event, or at any other time following its intrusion. As discussed in Section 2, in the absence of evidence for deformation or recrystallization we consider the myrmekitic textures to have formed at temperatures only just below the solidus temperature, such that all of the observed microstructural features formed well above the accepted maximum closure temperature for argon loss (~ 350-400°C).

6.2 MDD modelling

The Dead Fox K-feldspar does not show any of the characteristics that may prohibit the successful application of the MDD model, such as excessive low-Temperature and/or high-Temperature excess argon, or intermediate age maxima (Lovera et al., 2002). Moreover, there is a very good correlation between the age spectrum and the calculated $\log(r/r_0)$ plot (Fig. 7), a comparison with which we are able to assess the degree to

366 which the age spectra and ^{39}Ar release spectra are compatible with volume diffusion
367 (Lovera et al., 2002). Note that the $\log(r/r_0)$ plot is a representation of the domain size
368 distribution relative to the volume fraction of ^{39}Ar released (Lovera et al. 1991). The y-
369 axis, $\log(r/r_0)$, represents the size of the domains contributing ^{39}Ar at each stage in the
370 experiment, relative to the reference length scale, r_0, defined from the initial gas release
371 to which all domains contribute. The calculated correlation coefficient (C_{fg}) between the
372 age spectrum and the $\log(r/r_0)$ plot, as defined by Lovera et al. (2002), is high at 0.95.
373 Together these observations suggest that the MDD method may be appropriately
374 applied to this sample.

375 The model produces a good fit to the laboratory Arrhenius and $\log(r/r_0)$ data
376 and the resultant thermal history produces a good fit to the laboratory age spectrum
377 (Fig. 7). The activation energy (E_a) is calculated using the initial low-temperature gas
378 release, as defined by the linear portion of the Arrhenius array (Fig. 7b). The activation
379 energy of 58 kcal/mol calculated for Dead Fox K-feldspar is high compared to the
380 global average K-feldspar value of 46 ± 6 kcal/mol, however it is still within the range
381 for K-feldspar of ~ 30-70 kcal/mol reported by Lovera et al. (1997). We suggest this
382 value is representative given that there is no evidence for contamination of the mineral
383 separate and that repeat diffusion experiments on different aliquots and all give E_a = 58
384 ± 2 kcal/mol.

385 The resultant thermal history modelling gives a family of possible temperature-
386 time paths (Fig. 7) that appear plausible given constraints on the regional tectonic and
387 thermal histories available from the nearby Arunta and Tanami Inliers. The modelled
388 thermal history predicts three major periods of cooling: (1) rapid cooling from around
389 1580 Ma until 1500 Ma; (2) cooling between ~ 1000 and 850 Ma and, (3) final cooling
390 between 800 and 450 Ma. The exact timing of final cooling cannot be determined due to
391 the excess argon contamination of the early released gas. Cooling between around 1580
392 Ma and 1500 Ma is consistent with the known age of the Chewings Orogeny. Cooling
393 commencing just prior to 1000 Ma may be associated with unroofing due to extension
394 associated with the intrusion of the Stuart and Kulgera Dyke swarms (e.g., Zhao and
395 McCulloch, 1993) immediately prior to the formation of the Centralian Superbasin
396 (Walter et al., 1995). Although we are unable to constrain the timing of cooling precisely

from this sample alone, we note that a similar record of cooling in the interval 1000-800 Ma is apparently recorded by a number of other K-feldspars from northern central Australia (S. McLaren, G. Fraser, unpublished data).

The MDD modelling makes predictions about the size of "domains" and the volume fractions of argon they contain from the nature of the ^{39}Ar release pattern (Fig. 7; Table 3). The automated MDD modelling routines can produce a set of up to 10 different domain distributions which, for the Dead Fox K-feldspar, each provide slightly different fits to the observed Arrhenius and $\log(r/r_0)$ data. Lovera et al., (1991) have shown that although the release of ^{39}Ar during step heating does not allow the domain distribution to be determined uniquely, differences in the number of domains or their geometry do not significantly affect the modelled thermal history. For our purposes however, we are interested in at least the *range* of size and volume fraction of the predicted domain distribution. In our discussion we only include results from the peak best-fit solution (Table 3), which, based on the fits to the laboratory data, is considered to provide the best description of the domain structure.

The predicted domain distribution comprises 8 domains that vary in size by a factor of 1800. However, as they are very similar in size, domains 3 and 4 and 5 and 6 can be combined without any degradation of the model result, meaning that our distribution contains only 6 distinct domain sizes (Table 3). A key feature of this simplified 6-domain distribution is the presence of two domains, which we label C and F, and which together account for more than 60% of the total gas release (Table 3). Domain F is the largest domain size in the sample (relative domain size = 1.0) and contains ~ 23% of the total gas released. Domain C, the smaller of the two dominant domains is around $1/17^{th}$ of the size of Domain F and contains almost 41% of the total gas released. The smallest domains (relative size = 0.00055 and 0.0023) together contain ~ 16 % of the total gas and the remaining 21% of the gas released is predicted to have come from two intermediate sized domains with relative sizes ~ 0.21 and 0.31.

6.3 *In situ UV $^{40}Ar/^{39}Ar$ dating*

We have attempted to link the ages recorded in the age spectrum to the microstructural domains characterised by orientation variations using the ultra-violet laser ablation microprobe. The primary drawback of in-situ $^{40}Ar/^{39}Ar$ analysis using UV laser heating is the preferential loss of excess argon from defects, dislocations and the decrepitation of fluid inclusions (e.g. Burgess et al., 1992, Mulch et al., 2002). We experienced some problems with excess argon contamination leading to artificially old ages in excess of the intrusive age of the granite. However, we were able to successfully obtain ages that were not obviously contaminated by excess argon, that is, ages within the range recorded in the age spectrum (Fig. 8, Fig. 9). Partly as a result of the problems we encountered with excess argon contamination, we were particularly interested in identifying candidate microstructural domains to account for the youngest and oldest ages recorded.

Sub-micron scale features that we could not characterize using the EBSD method, and for which we cannot obtain age information, are likely candidates for the smallest domains in the model domain distribution (with relative size 0.00055 – 0.0023 in this example). The relative size of these features is probably related to crystallographic structure and, as such, are is likely to be similar to those previously characterized by transmission electron microscopy in other samples (e.g. Fitz Gerald and Harrison, 1993).

Our microstructural observations suggest that the grain-mosaic K-feldspars (as described in Section 2.3) are the next smallest coherent "domain" candidate that we can observe on a scale > 1 μm. These grain-mosaic textured K-feldspars vary in diameter from around 20 – 50 μm (Fig. 8). Fig. 8 shows the location and size of the ablation pits and $^{40}Ar/^{39}Ar$ ages for these analyses, together with the EBSD orientation contrast images. The youngest ages recorded are 701 ± 168 Ma, 791 ± 180 Ma and 815 ± 175 Ma, which are all within error of one another and which correspond well to the youngest ages recorded in the age spectrum (Fig. 8). The large errors on the ages are largely attributable to the very small volumes of gas released. However, at least two of the ablation pits appear to sample smaller K-feldspar grains around 5 μm in diameter with significant internal orientation contrast and which may represent more than one age

455 domain, with the smaller sub-domains possibly characterized by even younger ages.
456 The sampling of multiple age domains in this way may also help to account for the
457 relatively high uncertainty on these ages.

458 In contrast to the young ages recorded by the small grain-mosaic K-feldspars,
459 large homogeneous regions of K-feldspar with apparently simple microstructure
460 appear to record old ages (1569 ± 18 Ma and 1465 ± 18 Ma) that correspond well with
461 the oldest ages recorded by the age spectrum (Fig. 9). These analyses suggest that in
462 otherwise homogeneous K-feldspar, regions of pristine and turbid material are not
463 characterized by significant differences in $^{40}Ar/^{39}Ar$ age. This observation is at least
464 consistent with the model of turbid K-feldspar forming under high-intermediate
465 temperature conditions (around 450°C; Parsons and Brown, 1984), above the closure
466 temperature of K-feldspar to argon loss. However, we recognize that even though these
467 ages do correspond to the oldest ages in the age spectrum, in reality the true gas age
468 may be younger and the ages we have measured could be contaminated by some
469 (small) component of older excess argon. In the case of the Dead Fox Granite K-
470 feldspars, very low total yield of ^{37}Ar and ^{38}Ar does not allow correction for chlorine-
471 derived excess argon. Unfortunately this inability to identify and/or correct for excess
472 argon from individual laser ablation microprobe $^{40}Ar/^{39}Ar$ analyses will also affect any
473 future attempts at high resolution dating of K-feldspars in this way.

474

475 7. Discussion

476 We have shown that automated electron backscatter diffraction analysis can be
477 successfully applied to K-feldspar. Appropriate choice of indexing parameters reduces
478 mis-indexing problems and allows the successful discrimination of co-existing K-
479 feldspar and plagioclase, despite the similarity of their electron-back-scattered patterns.
480 Quantitative crystallographic orientation data allows misorientations to be quantified,
481 revealing complex microstructural relationships even in undeformed K-feldspars.
482 Although in this study we have focussed on macroscopically undeformed samples, the
483 technique should be applicable to all feldspars and is likely to be potentially useful in
484 the analysis of deformation fabrics. Analysis of the deformation-related microstructure

485 of feldspar using EBSD has a number of benefits over other methods. In particular, the
486 EBSD method allows deformation-related microstructure to be characterized and
487 quantified on a large range of scales, in contrast to TEM that can only resolve sub-
488 micron scale variations in crystallographic orientation. The EBSD method also
489 compares favourably to the method proposed by Worden et al. (1994) in which cleavage
490 surfaces of feldspars are etched using dilute hydrofluoric acid and then viewed under
491 the scanning electron microscope. The etching method reveals only intracrystalline
492 boundaries and is incapable of quantifying any angular orientation variations, unlike
493 the EBSD method that allows identification of both boundaries and orientation
494 variations.

495 We have also shown that successful application of the EBSD method to alkali-
496 feldspar helps to provide quantitative constraints on the relationship between argon age
497 and orientation microstructure. The complexity of K-feldspar orientation variations
498 even within undeformed granitic feldspars, suggests that a literal interpretation of a
499 simple domain structure, as predicted by the MDD model, appears unlikely (see also
500 Reddy et al., 2001). However, we are able to recognize different sized microstructural
501 domains that appear to record at least a first order relationship with $^{40}Ar/^{39}Ar$ age. The
502 clear relationship between: (1) the largest microstructural "domains" and the oldest
503 $^{40}Ar/^{39}Ar$ apparent ages and (2) much smaller "domains" and much younger $^{40}Ar/^{39}Ar$
504 apparent ages, suggests that diffusion from different sized orientation domains is the
505 main control on argon loss in K-feldspar from the Dead Fox Granite. These results are
506 consistent with a microstructural control on multidomain diffusion and hence provide a
507 link between the disparate views of Parsons et al. (1999) and Lovera et al. (1989).

508 Grain mosaic K-feldspars associated with myrmekitization in the Dead Fox
509 Granite provide a clear candidate group for small to intermediate domains and have
510 $^{40}Ar/^{39}Ar$ ages corresponding to the young ages recorded in the age spectrum.
511 Fitz Gerald and Harrison (1993) were unable to find a candidate for these small to
512 intermediate domains in K-feldspar MH10, and our result is significant in possibly
513 representing the first identification of candidate domains for these size ranges. This size
514 range may correspond to model Domain C (Table 3). We also recognize clear candidate
515 groups for the largest domain size which record ages equivalent to the oldest ages in

516 the age spectrum (Fig. 9). These large domains may correspond to modelled Domain F
517 (Table 3). The relative dimensions of modelled Domains C and F vary by a factor of ~ 17
518 (Table 3) closely matching the relative dimensions of the candidate K-feldspars
519 identified by the microstructural analysis, at around 20-50 μm and around 350-1000 μm
520 respectively. Further work, involving microstructural 'mapping' of much larger areas
521 granite is required to ~~further~~ investigate this apparent correlation.

522 The role of sub-micron features has been emphasized by Parsons et al. (1999).
523 However, variations in the abundance and/or argon retention properties of sub-micron
524 features cannot explain the observed variations in $^{40}Ar/^{39}Ar$ apparent age reported
525 here. Unfortunately, limitations on the resolution of in-situ $^{40}Ar/^{39}Ar$ dating mean that
526 the ages of sub-micron scale microstructures cannot be constrained by this, or any other
527 study, without significant advances in analytical technique. A key point however, is
528 that if sub-micron scale microstructures are found throughout all feldspars at every
529 scale (Parsons et al., 1999), then their effect on the distribution of argon must be
530 essentially uniform. Thus, such features cannot explain argon heterogeneity within or
531 between K-feldspar grains at the scale of laser Ar analyses unless dislocations and low-
532 angle boundaries are responsible for the heterogeneous distribution of these sub-micron
533 features. This possibility has not yet been investigated. Simple microstructural
534 observations are likely to provide the most useful information on the nature and quality
535 of the thermochronologic information available from any given sample, and
536 microstructural examination should be an essential part of $^{40}Ar/^{39}Ar$ analysis.
537 Recrystallization and/or textural modification, which have been shown to affect the
538 distribution of argon, can generally be recognized using optical or conventional
539 scanning electron microscopy. For such samples proceeding to infer the precise form of
540 the cooling history via the MDD model cannot be recommended. Moreover, the wide
541 range in ages recorded by spot analyses of individual K-feldspars in this study suggests
542 that furnace step heating, rather than laser ablation $^{40}Ar/^{39}Ar$ analysis, is most
543 appropriate for routine age determinations of K-feldspar.

544

Acknowledgments

Geoff Fraser, John Fitz Gerald, Jim Dunlap and Mark Harrison are thanked for helpful discussions throughout the project. Geoff Fraser is also thanked for providing the Dead Fox Granite sample. Oscar Lovera provided initial assistance with the MDD modelling. We are grateful to Ian Parsons for his detailed comments on an earlier version of this manuscript. We are also grateful to Jo Wartho for assistance and guidance with UV $^{40}Ar/^{39}Ar$ analysis. Nick Timms and Rob Hough are thanked for help with sample preparation and Elaine Miller is thanked for assistance with SEM operation. Irradiation of the Dead Fox Granite K-feldspar grain separate was undertaken by the Australian Nuclear Science and Technology Organization, through the Australian Institute of Nuclear Science and Engineering and was analysed at the Research School of Earth Sciences. The ultra-violet laser ablation microprobe $^{40}Ar/^{39}Ar$ analyses were undertaken at the Western Australian Argon Isotope Facility, operated by a consortium consisting of Curtin University and the University of Western Australia. We are grateful to Mark Pearce and an anonymous reviewer for their comments on the manuscript. SM acknowledges the support of Australian Research Council Australian Postdoctoral Fellowship and Discovery Grant DP0208837. SMR acknowledges a Curtin University Targeted Research Fellowship and ARC Discovery Project DP0664078. This paper is TIGeR contribution XXX.

Appendix – $^{40}Ar/^{39}Ar$ Analytical Procedures

A K-feldspar mineral separate (sized between 300-450 μm) from the Dead Fox Granite sample was obtained using routine heavy liquid flotation and magnetic methods. The sample was concentrated to better than 99% purity with the principal impurities being mineral and fluid inclusions. The sample was irradiated for 672 hours in facility X33 (or X34) of the Australian Nuclear Science and Technology Organization HIFAR reactor, Lucas Heights, NSW, Australia. The K-feldspar was packed in an aluminium can with a number of samples of the fluence monitor GA1550 biotite (with K/Ar age 98.79 Ma, McDougall and Roksandic, 1974; Renne et al., 1998). The sample can was inverted 180^{o} three times during the irradiation to minimize the effect of the large neutron flux gradient along the length of the can and a cadmium liner was used to minimize interference from thermal neutrons. The sample was analysed at the Australian

National University. During the step-heating experiment the temperature was monitored using a thermocouple at the base of a tantalum crucible within a double-vacuum resistance furnace. The heating schedule comprised a series of 43 steps at temperatures between 450°C and 1450°C (including many duplicate and triplicate isothermal steps; *Supplementary Data Table 1*). After each heating step, the gas released was exposed to Zr-Al getters for ~ 10 minutes to remove all active gases. Purified argon was analysed using a VG Isotech MM3600 gas source mass spectrometer. Measurement was made using a Daly collector and photomultiplier with overall sensitivity of 3.5 x10^{-17} mol/mV. Corrections for argon produced by interactions of neutrons with K and Ca were made (Tetley et al., 1980). The ^{40}K abundance and decay constants were taken from standard values recommended by the IUGS Subcommission on Geochronology (Steiger and Jäger, 1977).

In situ ^{40}Ar/^{39}Ar analysis was undertaken at the Western Australian Argon Isotope facility, part of the John de Laeter Centre for Mass Spectrometry, at Curtin University operated by a consortium consisting of Curtin University at The University of Western Australia. Samples, that had previously been characterized using electron backscatter diffraction, were analysed in situ in thin section. The polished thick sections (~ 300 μm thickness) were removed from their glass slides and cleaned using ultrasonic treatment in methanol and subsequently deionised water. Regions of interest around 10 mm x 10 mm were broken off the polished section, individually wrapped in aluminium foil and loaded into an aluminium canister. Biotite age standard Tinto B (K-Ar age of 409.24 ± 0.71 Ma; Rex and Guise, 1995) was loaded at 5 mm intervals along the package to monitor the neutron flux gradient. The package was Cd-shielded and irradiated in the 5C position of the McMaster University Nuclear Reactor, Hamilton, Canada for 89 hours. Upon return of the material to Curtin University, the samples were loaded into an ultra-high vacuum laser chamber with a Suprasil 2 viewport and baked to 120°C overnight to remove adsorbed atmospheric argon from the samples and chamber walls.

Material was ablated using a New Wave Research LUV 213X 4 mJ pulsed quintupled Nd-YAG laser (λ = 213 nm) with a variable spot size of 20-350 μm, and a repetition rate of 10 Hz. The laser was fired through a Merchantek computer-controlled x-y-z sample chamber stage and microscope system, fitted with a high-resolution CCD

607 camera, 6x computer controlled zoom, high magnification objective lens, and two light
608 sources for sample illumination. Samples were ablated for approximately 10 seconds
609 and the gases released were 'gettered' using 3 SAES AP10 getter pumps to remove all
610 active gases. Remaining noble gases were equilibrated into a high sensitivity mass
611 spectrometer (MAP 215-50) operated at a resolution of 600 and fitted with a Balzers SEV
612 217 multiplier. The automated extraction and data acquisition system was computer
613 controlled, using a LabView program. The mean 3 minute extraction system blank Ar
614 isotope measurements (appropriate for spot analyses) obtained during the experiments
615 were 1.56×10^{-12}, 1.26×10^{-14}, 3.38×10^{-15}, 4.87×10^{-14} and 1.83×10^{-14}, cm^3 STP for ^{40}Ar,
616 ^{39}Ar, ^{38}Ar, ^{37}Ar and ^{36}Ar respectively. Samples were corrected for mass spectrometer
617 discrimination and nuclear interference reactions. Errors quoted on the ages are 1
618 sigma. $^{40}Ar/^{39}Ar$ ages were calculated using the decay constants of Steiger and Jäger
619 (1977).
620

621 # References

622 Bestmann, M., Prior, D.J., 2003. Intragranular dynamic recrystallization in naturally deformed
623 calcite marble: diffusion accommodated grain boundary sliding as a result of subgrain
624 rotation recrystallization. Journal of Structural Geology 25, 1597-1613
625 Budd, A.R., Wyborn, L.A.I., Bastrakova, I.V., 2001. The Metallogenic Potential of Australian
626 Proterozoic Granites. Geoscience Australia Record 2001/12
627 Burgess, R., Kelley, S.P., Parsons, I., Walker, F.D.L., Worden, R.H., 1992. $^{40}Ar/^{39}Ar$ analysis of
628 Perthite microtextures and fluid inclusions in alkali feldspars from the Klokken Syenite,
629 South Greenland. Earth and Planetary Science Letters 109, 147-167.
630 Castle, R.O., Lindsley, D.H. 1993. An exsolution silica-pump model for the origin of myrmekite.
631 Contributions to Mineralogy and Petrology 115, 58-65
632 Chichagov, A.V., Varlamov, D.A., Dilanyan, R.A., Dokina, T.N., Drozhzhina, N.A.,
633 Samokhvalova, O.L., Ushakovskaya, T.V., 2001. MINCRYST: A crystallographic database for
634 minerals, local and network (WWW) versions. Crystallography Reports 46, 876-879
635 Corsetti, F.A., Stewart, J.H., Hagadorn, J.W., 2006. Neoproterozoic diamictite-cap carbonate
636 succession and $\delta^{13}C$ chemostratigraphy from eastern Sonora, Mexico. Chemical Geology

237, 129-142.

Dunlap, W.J., Fossen, H., 1998. Early Paleozoic orogenic collapse, tectonic stability, and late Paleozoic continental rifting revealed through thermochronology of K-feldspars, southern Norway. Tectonics 17, 604-620

Elkins, L.T., Grove, T.L., 1990. Ternary feldspar experiments and thermodynamic models. American Mineralogist 75, 544-559.

Faul, U.H., Fitz Gerald, J.D., 1999. Grain misorientations in partially molten olivine aggregates: an electron back scattered diffraction study. Physics and Chemistry of Minerals 26, 187-197

Fitz Gerald, J.D., Harrison, T.M., 1993. Argon diffusion domains in K-feldspar I: microstructures in MH-10. Contributions to Mineralogy and Petrology 113, 367-380

Fitz Gerald, J.D., Parsons, I., Cayzer, N., 2006. Nanotunnels and pull-aparts: Defects of exsolution lamellae in alkali feldspars. American Mineralogist 91, 772-783.

Gatehouse, C.G., Fanning, C.M., Flint, R.B., 1995. Geochronology of the Big Lake Suite, Warburton Basin, northeastern South Australia. Quarterly Geological Notes of the Geological Survey of South Australia 128, 8-16

Hand, M., Buick, I., 2001. Tectonic evolution of the Reynolds-Anmatjira ranges; a case study in terrain reworking from the Arunta Inlier, central Australia. Special Publications of the Geological Society of London 184, 237-260

Harrison, T.M., Heizler, M.T., Lovera, O.M., Chen, W., Grove, M., 1994. A chlorine-disinfectant for excess argon released from K-feldspar during step-heating. Earth and Planetary Science Letters 123, 95-104

Hippertt, J.F., Valarelli, J.V., 1998. Myrmekite: constraints on the available models and a new hypothesis for its formation. European Journal of Mineralogy 10, 317-331

Hough P.V.C., 1962. Method and Means for Recognizing Complex Patterns. - U.S. Patent 3069354

Jiang, Z., Prior, D.J., Wheeler, J., 2000. Albite crystallographic preferred orientation and grain misorientation distribution in a low-grade mylonite: implications for granular flow. Journal of Structural Geology 22, 1663-1674

Lee, J.K.W., 1995. Multipath diffusion in geochronology. Contributions to Mineralogy and Petrology 120, 60-82

667 Lindsay, J.F., 1989. Depositional controls on glacial facies associations in a basinal setting, late
668 Proterozoic, Amadeus Basin, central Australia. Palaeogeography, Palaeoclimatology,
669 Palaeoecology 73, 205-232
670 Lovera, O.M., Richter, F.M., Harrison, T.M., 1989. The $^{40}Ar/^{39}Ar$ thermochronometry for slowly
671 cooled samples having a distribution of diffusion domain sizes. Journal of Geophysical
672 Research 94, 17917-17935
673 Lovera, O.M., Richter, F.M., Harrison, T.M., 1991. Diffusion domains determined from ^{39}Ar
674 released during step-heating. Journal of Geophysical Research 96, 2057-2069
675 Lovera, O.M., Grove, M., Harrison, T.M., Mahon, K.I., 1997. Systematic analysis of K-feldspar
676 $^{40}Ar/^{39}Ar$ step heating results: I. Significance of activation energy determinations. Geochimica
677 et Cosmochimica Acta 61, 3171-3192
678 Lovera, O.M., Grove, M., Harrison, T.M., 2002. Systematic Analysis of K-feldspar $^{40}Ar/^{39}Ar$ Step
679 Heating Results II: Relevance of Laboratory Argon Diffusion Properties to Nature.
680 Geochimica et Cosmochimica Acta 66, 7, 1237-1255
681 McDougall, I., 1985. K-Ar and $^{40}Ar/^{39}Ar$ dating of the hominid-bearing Pliocene-Pleistocene
682 sequence at Koobi Fora, Lake Turkana, northern Kenya. Geological Society of America
683 Bulletin 96, 159-175.
684 McDougall, I., Roksandic, Z., 1974. Total fusion $^{40}Ar/^{39}Ar$ ages using HIFAR reactor. Journal of
685 the Geological Society of Australia 21, 81-89
686 McLaren, S., Dunlap, W.J., 2006. The use of $^{40}Ar/^{39}Ar$ K-feldspar thermochronology in basin
687 thermal history reconstruction: an example from the Big Lake Suite granites, Warburton
688 Basin, South Australia. Basin Research 18: 189-203, doi:10.1111/j.1365-2117.2006.00288.x
689 McLaren, S., Dunlap, W.J., Sandiford, M., McDougall, I., 2002. Thermochronology of high heat
690 producing crust at Mount Painter, South Australia: implications for tectonic reactivation of
691 continental interiors. Tectonics 21, 4, 10.1029/2000TC001275
692 Mulch, A., Cosca, M.A., Handy, M.R., 2002. In-situ UV-laser $^{40}Ar/^{39}Ar$ geochronology of a
693 micaceous mylonite: an example of defect-enhanced argon loss. Contributions to Mineralogy
694 and Petrology 142, 738-752
695 Page, R., 1996. Sample 2000082040. Unpublished data in Geoscience Australia OZCHRON
696 geochronology database. http://www.ga.gov.au

697 Parsons, I., Brown, W.L., 1984. Feldspars and the thermal history of igneous rocks. In: Brown
698 WL (Ed.) Feldspars and feldspathoids: structure, properties and occurrences, p. 317-371.
699 NATO ASI Series C. Reidel Publishing, Dordrecht
700 Parsons, I., Brown, W.L., Smith, J.V., 1999. $^{40}Ar/^{39}Ar$ thermochronology using alkali feldspars:
701 real thermal history or mathematical mirage of microtexture? Contributions to Mineralogy
702 and Petrology 136, 92-110
703 Prince, E., Donnay, G., Martin, R.F., 1973. Neutron diffraction refinement of an ordered
704 orthoclase structure. American Mineralogist 58, 500-509
705 Prior, D.J., Wheeler, J., 1999. Feldspar fabrics in a greenschist facies albite-rich mylonite from
706 electron backscatter diffraction. Tectonophysics 303, 29-49
707 Prior, D.J., Trimby, P.W., Weber, U.D., 1996. Orientation contrast imaging of microstructures in
708 rocks using forescatter detectors in the scanning electron microscope. Mineralogical
709 Magazine 60, 859-869
710 Prior, D.J., Boyle, A.P., Brenker, F., Cheadle, M.C., Day, A., Lopez, G., Peruzzo, L., Potts, G.J.,
711 Reddy, S., Spiess, R., Timms, N.E., Trimby, P., Wheeler, J., Zetterström, L., 1999. The
712 application of electron backscatter diffraction and orientation contrast imaging in the SEM to
713 textural problems in rocks. American Mineralogist 84, 1741-1759
714 Prior, D.J., Wheeler, J., Peruzzo, L., Spiess, R., Storey, C., 2002. Some garnet microstructures; an
715 illustration of the potential of orientation maps and misorientation analysis in
716 microstructural studies. Journal of Structural Geology 24, 999-1011
717 Pryer, L.L., Robin, P-Y.F., Lloyd, G.E., 1995. An SEM electron-channelling study of flame
718 perthite from the Killarney Granite, South-Western Grenville Front, Ontario. Canadian
719 Geologist 33, 333-347
720 Randle, V., 2000. Theoetical framework foe electron backscatter diffraction. In SwartzAJ, Kumar
721 M, Adams BL, (eds) Electron Backscatter Diffraction in Materials Science. Kluwer Academic,
722 New York, pp. 19-30
723 Reddy, S.M., Potts, G.J., Kelley, S.P., Arnaud, N.O., 1999. The effects of deformation-induced
724 microstructures on intragrain $^{40}Ar/^{39}Ar$ ages in potassium feldspar. Geology 27, 363-366
725 Reddy, S.M., Potts, G.J., Kelley, S.P., 2001. $^{40}Ar/^{39}Ar$ ages in deformed potassium feldspar:
726 evidence of microstructural control on Ar isotope systematics. Contributions to Mineralogy
727 and Petrology 141, 186-200

728 Reddy, S.M., Timms, N.E., Trimby, P., Kinny, P.D., Buchan, C., Blake, K., 2006. Crystal-plastic
729 deformation of zircon: A defect in the assumption of chemical robustness. Geology 34, 257-
730 260.
731 Reddy, S.M., Timms, N.E., Pantleon, W., Trimby, P. 2007. Quantitative characterization of
732 plastic deformation of zircon and geological implications. Contributions to Mineralogy and
733 Petrology 153, 625-645.
734 Reddy, S.M., Timms, N.E. & Eglington, B.M. 2008. Electron backscatter diffraction analysis of
735 zircon: A systematic assessment of match unit characteristics and pattern indexing
736 optimization. American Mineralogist, 93, 187-197.
737 Renne, P.R., Swisher, C.C., Deino, A.L., Karner, D.B., Owens, T.L., DePaolo, D.J., 1998.
738 Intercalibration of standards, absolute ages and uncertainties in $^{40}Ar/^{39}Ar$ dating. Chemical
739 Geology 145, 117-152
740 Rex, D.C., Guise, P.G., 1995. Evaluation of argon standards with special emphasis on time scale
741 measurement. In: Odin GS (Ed.) Phanerozoic Time Scale. Bull Liais Inform IUGS
742 Subcomission Geochronology 13: 21-23
743 Richter, F.M., Lovera, O.M., Harrison, T.M., Copeland, P., 1991. Tibetan tectonics from $^{40}Ar/^{39}Ar$
744 analysis of a single K-feldspar sample. Earth and Planetary Science Letters 105, 266-278
745 Skrotzki, W., Tamm, R., Oertel, C-G., Roseberg, J., Brokmeier, H-G., 2000. Microstructure and
746 texture formation in extruded lead sulfide (galena). Journal of Structural Geology 22, 1621-
747 1632
748 Spell, T.L., McDougall, I., Doulgeris, A.P., 1996. Cerro Toledo Rhyolite, Jemez Volcanic Field,
749 New Mexico: $^{40}Ar/^{39}Ar$ geochronology of eruptions between two caldera-filling events.
750 Geological Society of America Bulletin 108, 1549-1566
751 Steiger, R., Jäger, E., 1977. Subcommission on geochronology: Convention on the use of decay
752 constants in geo- and cosmochronology. Earth and Planetary Science Letters 36, 359-362
753 Swisher, C.C. III, Dungus, L., Butler, R.F., 1993. $^{40}Ar/^{39}Ar$ dating and magnetostratigraphic
754 correlation of the terrestrial Cretaceous-Paleogene boundary and Puercan Mammal Age, Hell
755 Creek-Tullock formations, eastern Montana. Canadian Journal of Earth Sciences 30, 1981-
756 1996
757 Sun, X., 1997. Structural style of the Warburton Basin and control in the Cooper and Eromanga
758 Basins, South Australia. Exploration Geophysics 28, 333-339

759 Tetley, N., McDougall, I., Heydegger, H.R., 1980. Thermal neutron interferences in the $^{40}Ar/^{39}Ar$
760 dating technique. Journal of Geophysical Research 85, 7201-7205
761 Teyssier, C., Amri, C., Hobbs, B.E., 1988. South Arunta Block: the internal zones of a Proterozoic
762 overthrust in central Australia. Precambrian Research 40/41, p. 157-173.
763 Waldron, K., Lee, M.R., Parsons, I., 1994. The microstructures of perthitic alkali-feldspars
764 revealed by hydrofluoric acid etching. Contributions to Mineralogy and Petrology 116, 360-
765 364.
766 Walter, M.R., Veevers, J.J., Calver, C.R., Grey, K., 1995. Neoproterozoic stratigraphy of the
767 Centralian Superbasin, Australia. Precambrian Research 73, 173-195
768 Wartho, J-A., Kelley, S.P., Booker, R.A., Carroll, M.R., Villa, I.M., Lee, M.R., 1999. Direct
769 measurement of Ar diffusion profiles in a gem-quality Madagascar K-feldspar using the
770 ultra-violet laser ablation microprobe (UVLAMP). Earth and Planetary Science Letters 170,
771 141-153
772 Williame, C., Brown, W.L., 1974. A coherent elastic model for the determination of the
773 orientation of exsolution boundaries: application to feldspars. Acta Crystllographica 30, 316-
774 331.
775 Winter, J.K., Okamura, F.P., Ghose, S., 1979. A high-temperature structural study of high albite,
776 monalbite, and the analbite - monalbite phase transition. American Mineralogist 64, 409-423.
777 Wyborn, L.A.I., Ord, A., Hobbs, B., Idnurm, M., 1997. Australian Geological Survey
778 Organization Record 1997/44, p. 131-134
779 Zhao, J-X., McCulloch, M.T., 1993. Sm-Nd mineral isochron ages of late Proterozoic dyke
780 swarms in Australia; evidence for two distinctive events of mafic magmatism and crustal
781 extension. Chemical Geology 109, 341-354
782

Figure Captions

Figure 1. Transmitted light micrographs of myrmekitic alkali-feldspar textures in the Dead Fox Granite (a) large single K-feldspar grain surrounded by moat of myrmekitic quartz, plagioclase and K-feldspar, (b) myrmekitic reaction front between K-feldspar and plagioclase grains, (c) similar view to (b) showing individual grain mosaic K-feldspars within the myrmekitic texture; (d) rare large K-feldspar grain showing well developed cross-hatched 'tartan' twinning; dashed lines outline regions of turbidity.

Figure 2. Examples of empirically obtained electron backscatter patterns (EBSPs) together with the fit to theoretical reflector files (draped over the original EBSP) for (a) K-feldspar and (b) Plagioclase. Two diagnostic bands that allow the patterns to be discriminated are highlighted.

Figure 3. Example of EBSD results from Sample 01-524, Areyonga Formation granitic K-feldspar, (a) grey scale ANC image (dark grey = plagioclase, light grey = K-feldspar), (b) band contrast image indicating the quality of the data points (c) electron backscatter diffraction phase map showing indexing of plagioclase (blue) and K-feldspar (green) via automatic mapping, (d) texture map showing a 10°misorientation variation, shown by the color bar, from the EBSP collected at the position of the red cross. , (e) Lower hemisphere equal area projections of {100}, {010} and {001} crystallographic poles for data shown in (d). Data show total misorientation across the mapped part of the grain of 17°. Colors correspond to those shown in (d).

Figure 4. Example of EBSD results from Sample 02-149, Big Lake Suite granitic K-feldspar. (a) grey scale ANC image (dark grey = plagioclase, light grey = K-feldspar), (b) band contrast image (c) electron backscatter diffraction phase map showing indexing of plagioclase (blue) and K-feldspar (green) via automatic mapping, (d) texture map showing a 3°misorientation variation, shown by the color bar, from the EBSP collected at the position of the red cross.

Figure 5. Example of EBSD results from Sample 02-149, Big Lake Suite granitic K-feldspar. (a) grey scale ANC image (dark grey = plagioclase, light grey = K-feldspar), (b) band contrast image (c) electron backscatter diffraction phase map, showing indexing of plagioclase (blue) and K-feldspar (green) via automatic mapping, (d) texture map showing a 3°misorientation variation, shown by the color bar, from the EBSP collected at the position of the red cross.

Figure 6. Measured $^{40}Ar/^{39}Ar$ age spectrum for K-feldspar from the Dead Fox Granite. Also indicated are the intrusion age (Zircon $^{207}Pb/^{206}Pb$ age) and the approximate age of the Chewings Orogeny (Teyssier et al., 1988; Hand and Buick, 2001).

Figure 7. Results of multiple-diffusion-domain modelling (a) measured and modelled age spectra (b) log r/r0 plots (c) measured and modelled Arrhenius data (d) preferred thermal histories

Figure 8. Dead Fox Granite (a) back scattered electron image showing atomic number contrast; note disrupted microstructures associated with myrmekitic intergrowths of K-feldspar, quartz and plagioclase; box shows location of (b); (b) Orientation contrast image showing coherent subgrain K-feldspar, subgrains range in size from ~ 15 to 60 μm and show little internal orientation contrast. Circles show the location and size of UV laser ablation pits and corresponding $^{40}Ar/^{39}Ar$ ages; (c) age spectrum from grain separate showing ages, with one sigma errors, recorded by the three youngest spot analyses; (d) Orientation contrast image with EBSD map overlain. EBSD map shows texture component and is shaded red-blue to represent a 60° orientation contrast from pixel indicated by the red cross.

Figure 9. Dead Fox Granite (a) ANC image showing atomic number contrast; (b) Orientation contrast image showing (1) area of macroscopically homogeneous K-feldspar characterized by only very subtle orientation contrasts and (2) area of turbid K-feldspar, characterized by small pits and holes and significant micron scale orientation contrast. Also shown are the location of the UV laser ablation pits and corresponding $^{40}Ar/^{39}Ar$ ages; (c) age spectrum from grain separate showing actual ages recorded by the two spot analyses; age of 2352 ± 38 Ma is older than the age of the granite and represents excess argon contamination.

833 **Table 1** Electron microprobe point analyses for individual feldspars
834

	K_2O	CaO	FeO	Fe_2O_3	BaO	Na_2O	MgO	Al_2O_3	SiO_2	Total
Dead Fox Granite	11.3019	0.0154	nd		0.3557	0.9459	0.0192	19.589	66.0658	98.2929
	11.3413	0.037	nd		0.3817	0.8926	0.0116	19.512	65.7536	97.9298
	11.3434	0.033	0.0004		0.3600	0.9421	nd	19.8205	65.4977	97.997
	11.3594	0.0252	0.0068		0.3855	0.9588	nd	19.7518	66.0949	98.5823
	11.4921	0.0026	0.0081		0.3946	0.7647	nd	19.648	65.6808	97.9909
	11.3449	0.0145	0.0039		0.3337	0.9814	nd	19.6819	66.6118	98.972
	11.3196	0.0266	0.0184		0.3258	1.0306	nd	19.8531	65.8768	98.4508
	11.3789	0.0197	0.0041		0.3226	0.9983	nd	19.449	65.648	97.8205
01-524	12.0986	0.0219	nd		0.0871	0.3758	0.0054	19.8005	65.3104	97.6997
	11.884	0.03	0.0313		0.0641	0.5131	0.0027	19.8104	64.1321	96.4677
	12.2487	nd	0.0049		0.0307	0.2	0.0177	19.7974	64.5125	96.8119
	12.2055	0.0148	nd		nd	0.3409	0.0041	19.8481	64.0276	96.441
	11.8982	0.0405	0.0056		0.0103	0.4654	0.0095	20.1106	63.8367	96.377
	12.0424	0.0412	0.0273		0.0116	0.4591	nd	20.0078	63.3243	95.9136
	11.8492	0.0212	0.0188		nd	0.5267	0.0034	20.1366	63.0283	95.5842
	11.9554	0.0188	0.0124		0.0077	0.4979	0.0116	20.1536	63.1732	95.8305
	11.9908	0.02	0.009		0.0434	0.5026	nd	20.0731	63.1294	95.7682
	12.1116	0.0121	0.0082		0.1279	0.3548	nd	19.9813	65.1167	97.7125
	0.054	0.413	0.0155		nd	10.8763	0.0058	21.4695	67.9193	100.7534
	0.0628	0.6001	0.1133		nd	10.7773	0.0044	21.4776	68.0796	101.1151
	0.0675	0.9075	0.0148		nd	10.5686	nd	21.816	67.3763	100.7507
02-149	15.9772	0.0434		0.0756	0.0166	0.896		18.2477	64.3588	99.6152
	16.3214	0.0176		0.0272	0.0277	0.6258		18.0662	64.3981	99.5737
	14.0948	0.023		0.0530	nd	1.6837		18.1095	64.2642	98.2282
	16.2271	0.0396		0.0212	0.0221	0.6378		18.2375	64.0496	99.2349
	16.8626	0.0159		0.0575	nd	0.2877		18.2839	64.3495	99.8911
	15.2475	0.0141		nd	0.0111	1.4299		18.1836	65.0951	99.9813
	15.5439	0.0293		0.0862	0.0498	1.1311		18.2912	64.0321	99.1635
	15.6341	0.0251		0.0650	0.0277	1.1512		18.31	63.7699	98.9892
	16.2978	0.019		nd	nd	0.4982		18.1694	64.0373	99.0217
	0.2609	1.6961		0.0852	nd	10.3391		21.0156	66.9047	100.321
	0.1954	0.0808		0.0107	0.0275	11.5064		19.2678	68.6355	99.7242
	0.2346	0.2131		0.0122	0.0771	11.1043		19.5654	68.4793	99.686
02-147	13.873	0.0271		0.1686	0.0054	1.0334		18.7846	63.5762	97.4684
	15.0604	nd		0.0015	0.0654	1.3669		18.3029	61.1327	95.9298
	16.7583	0.0131		nd	nd	0.1932		18.3867	64.9228	100.2958
	16.8522	nd		0.0333	0.0387	0.2471		18.5207	64.4575	100.1495
	16.9467	0.0116		0.0119	0.1529	0.1832		18.792	63.441	99.5668
	16.9883	nd		0.0149	nd	0.1797		18.3217	61.3782	96.9163
	16.9924	0.0017		0.0179	0.1799	0.1658		18.2864	62.0894	97.7334

835

836

837 **Table 2** Settings for EBSD acquisition and processing

838

	EBSD settings		
	Fig.3 b,c,d	***Fig. 4 b,c,d***	***Fig.5 b,c,d***
EBSP collection time (ms)	60	60	60
Background Correction # Frames	64	64	64
EBSP noise reduction - frames	4	4	4
- binning	4 x 4	4 x 4	4 x 4
- gain	Low	Low	Low
Band detection (min/max bands)	4/6	6/8	5/8
Hough resolution	65	60	65
MAD Threshold	1.50	1.50	1.50
X steps	150	100	79
Y steps	144	100	81
Step distance (µm)	3	3	2
Cycling time (s/pattern)	0.263	0.280	0.315
Project duration	1:34:32	0:46:44	0:33:36
Zero solutions (%)	3.9	3.4	3.3
NR - 'wildspike'	yes	yes	yes
- *n* neighbor zero solution	4	4	4
Albite %	27.7	39.2	15.0
Albite mean MAD	0.804	0.720	0.630
Orthoclase %	68.4	57.4	81.7
Orthoclase mean MAD	0.624	0.529	0.516

839

840

841 **Table 3** Calculated domain distribution for Dead Fox Granite K-feldspar
842

Domain	Log D_o cm^2s^{-1}	Volume fraction (%) ϕ_j	Domain Size (Relative) ρ_j	Simplified domain distribution
1	9.31640	8.630	0.00055	A
2	8.08063	7.114	0.00230	B
3	5.24300	24.050	0.06026	C
4	5.22013	16.852	0.06187	
5	4.16447	11.811	0.20859	D
6	4.14975	6.645	0.21216	
7	3.83160	2.311	0.30601	E
8	2.80306	22.588	1.00000	F

843

844

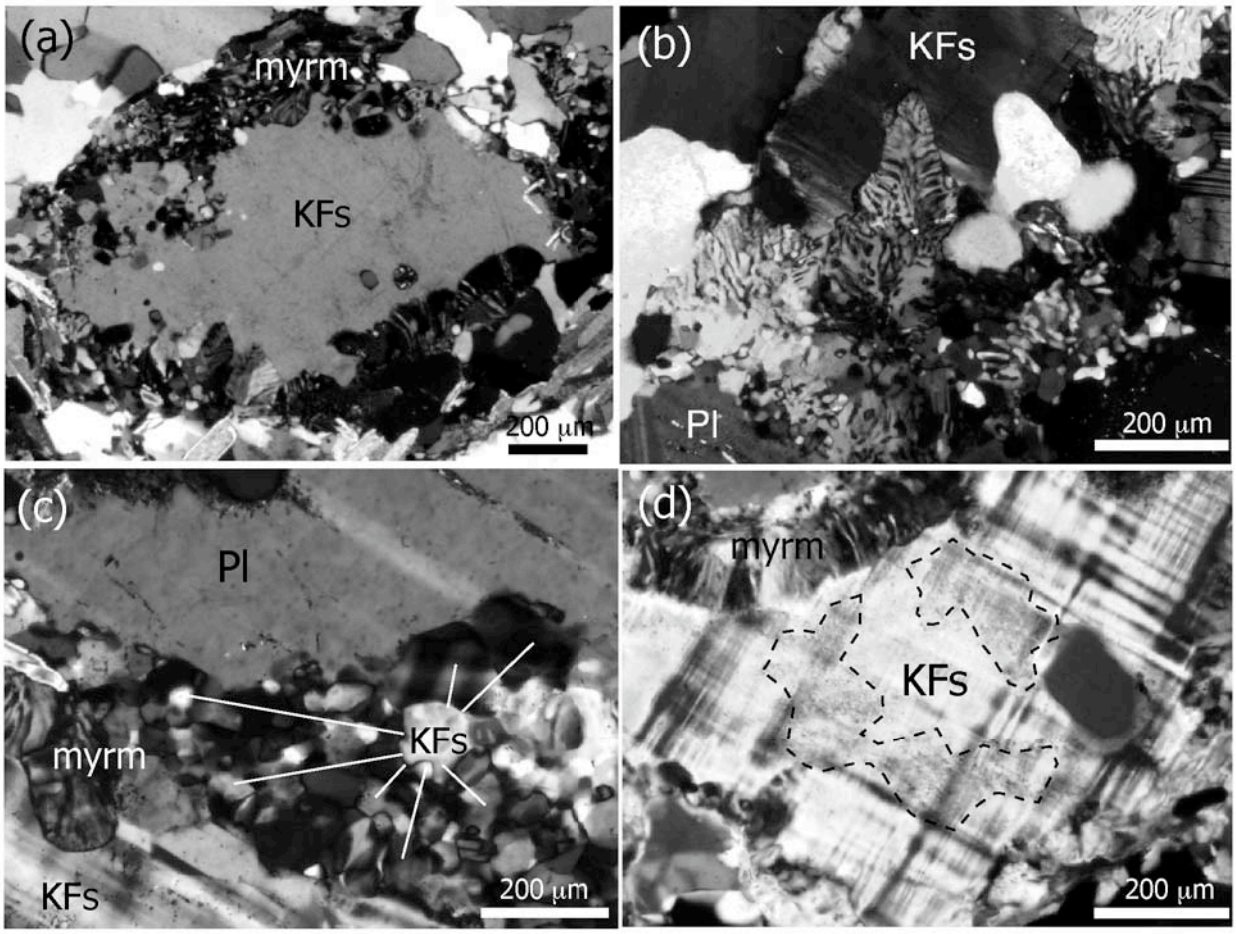
(a)
myrm
KFs
200 μm
(b)
KFs
Pl
200 μm
(c)
Pl
myrm
KFs
KFs
200 μm
(d)
myrm
KFs
200 μm

Figure 1

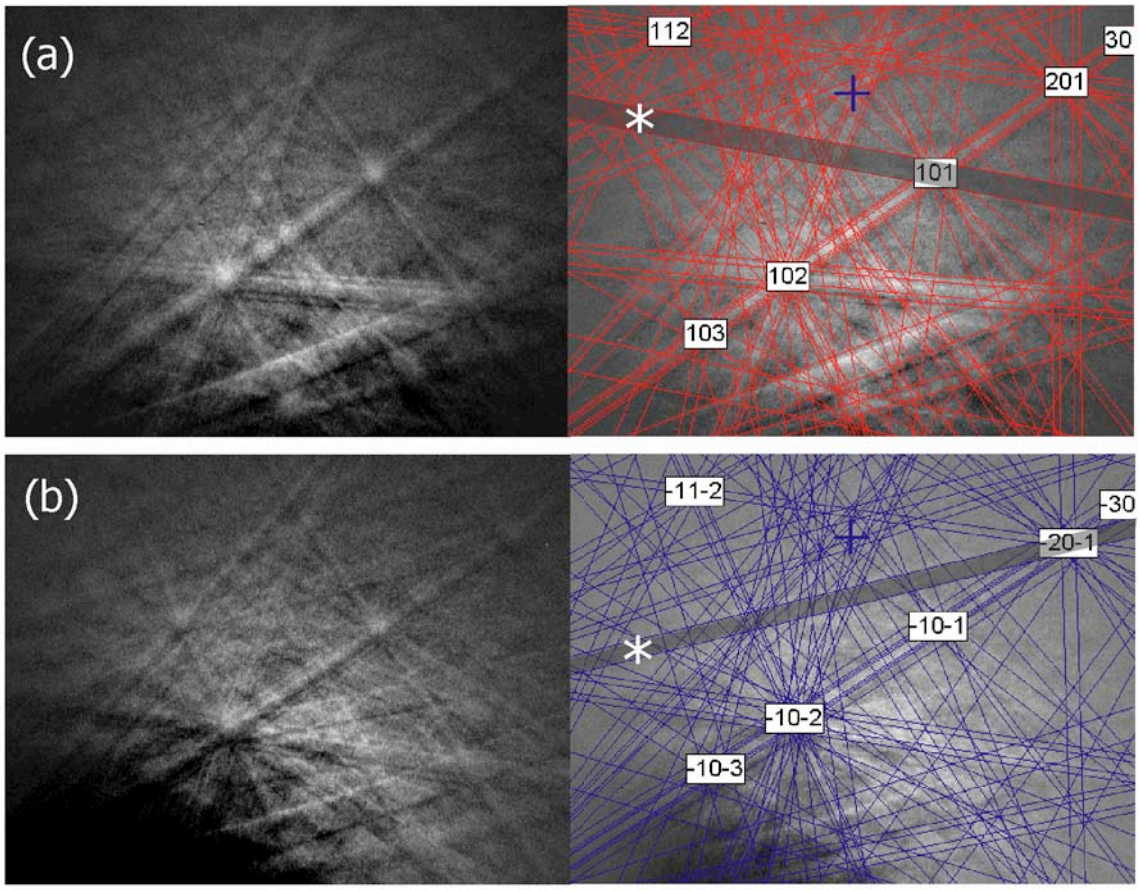

Figure 2

Figure 3

Click here to download high resolution image

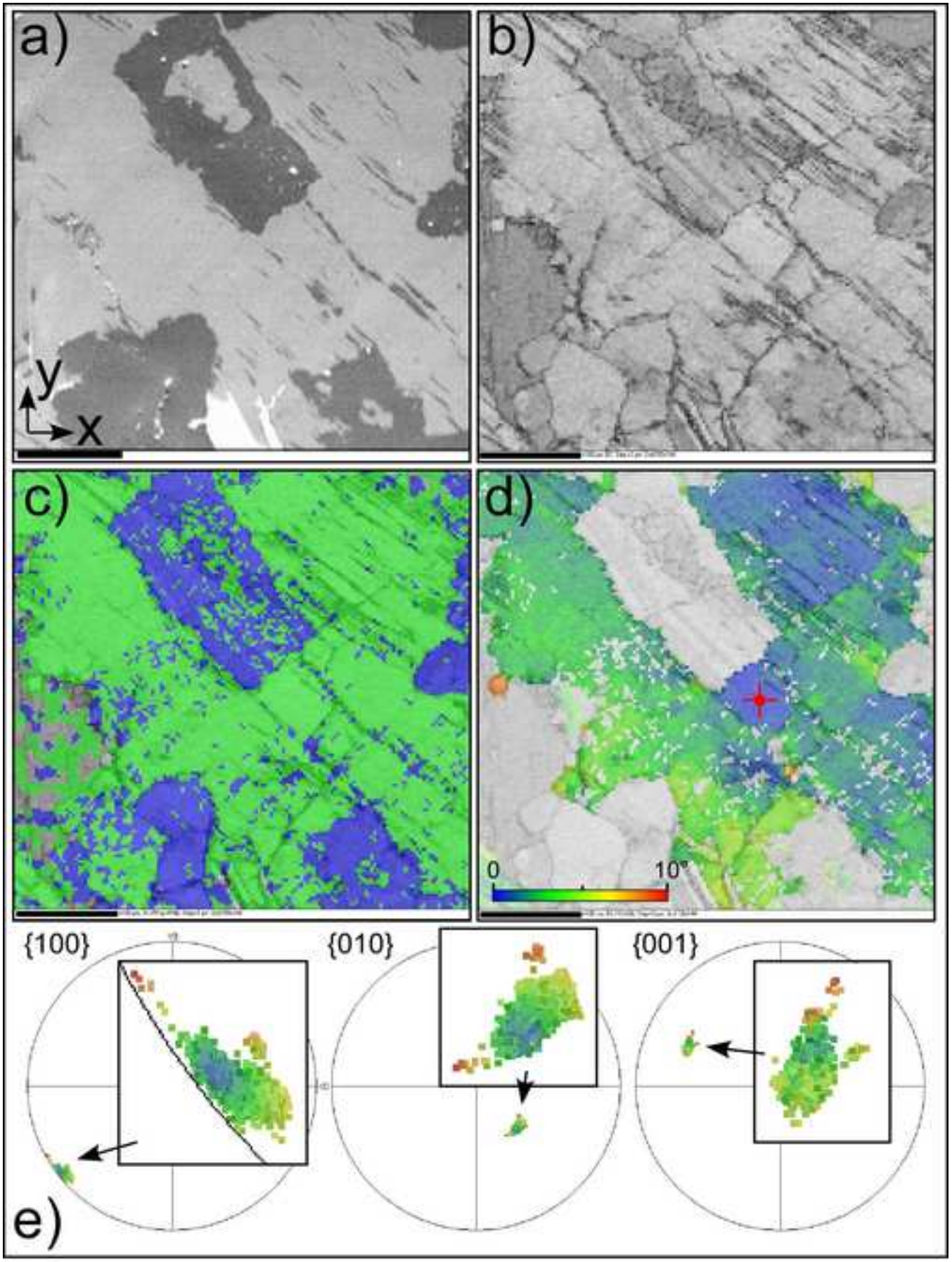

Figure 3

Figure 4

Click here to download high resolution image

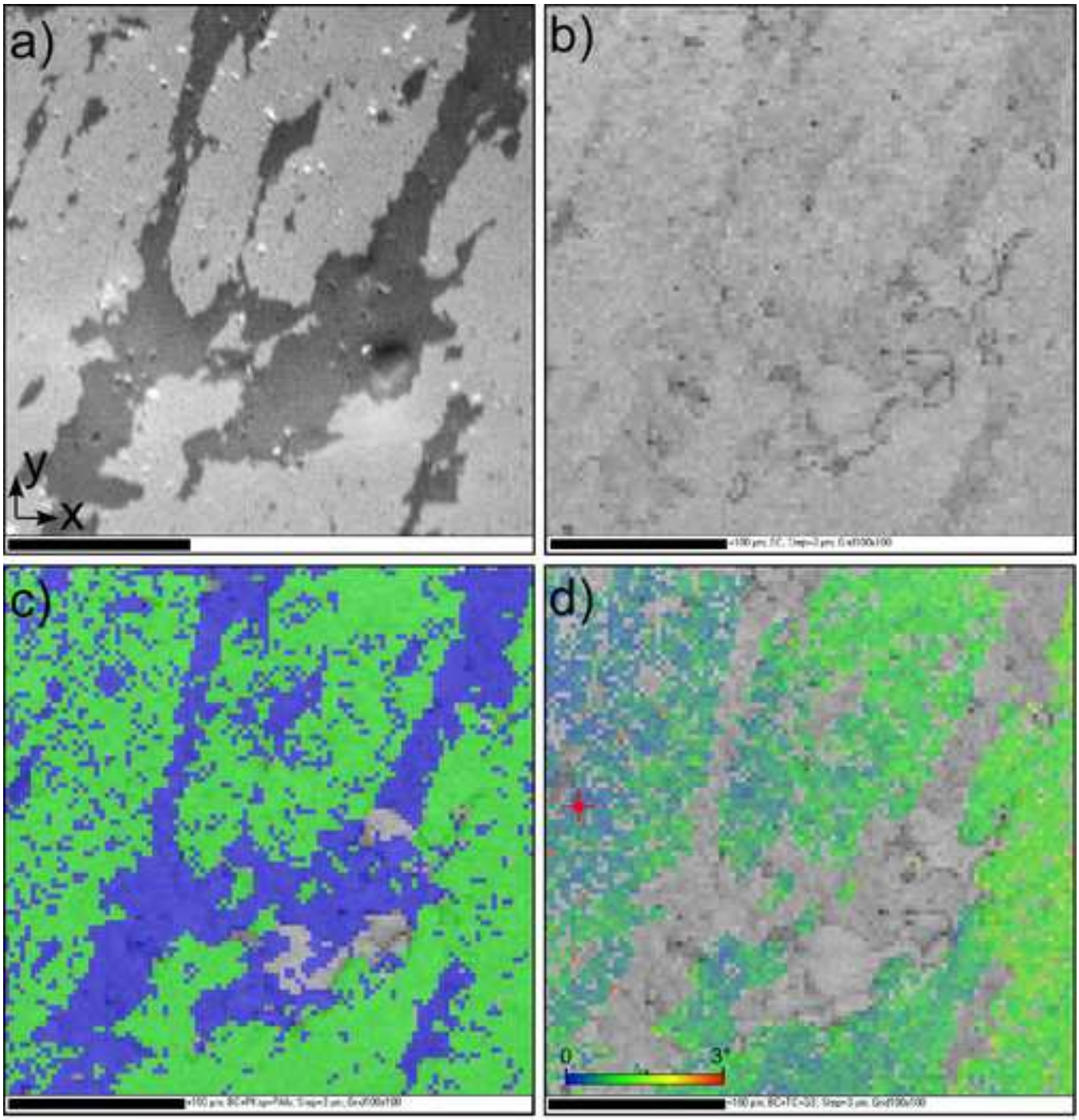

Figure 4

Figure 5
Click here to download high resolution image

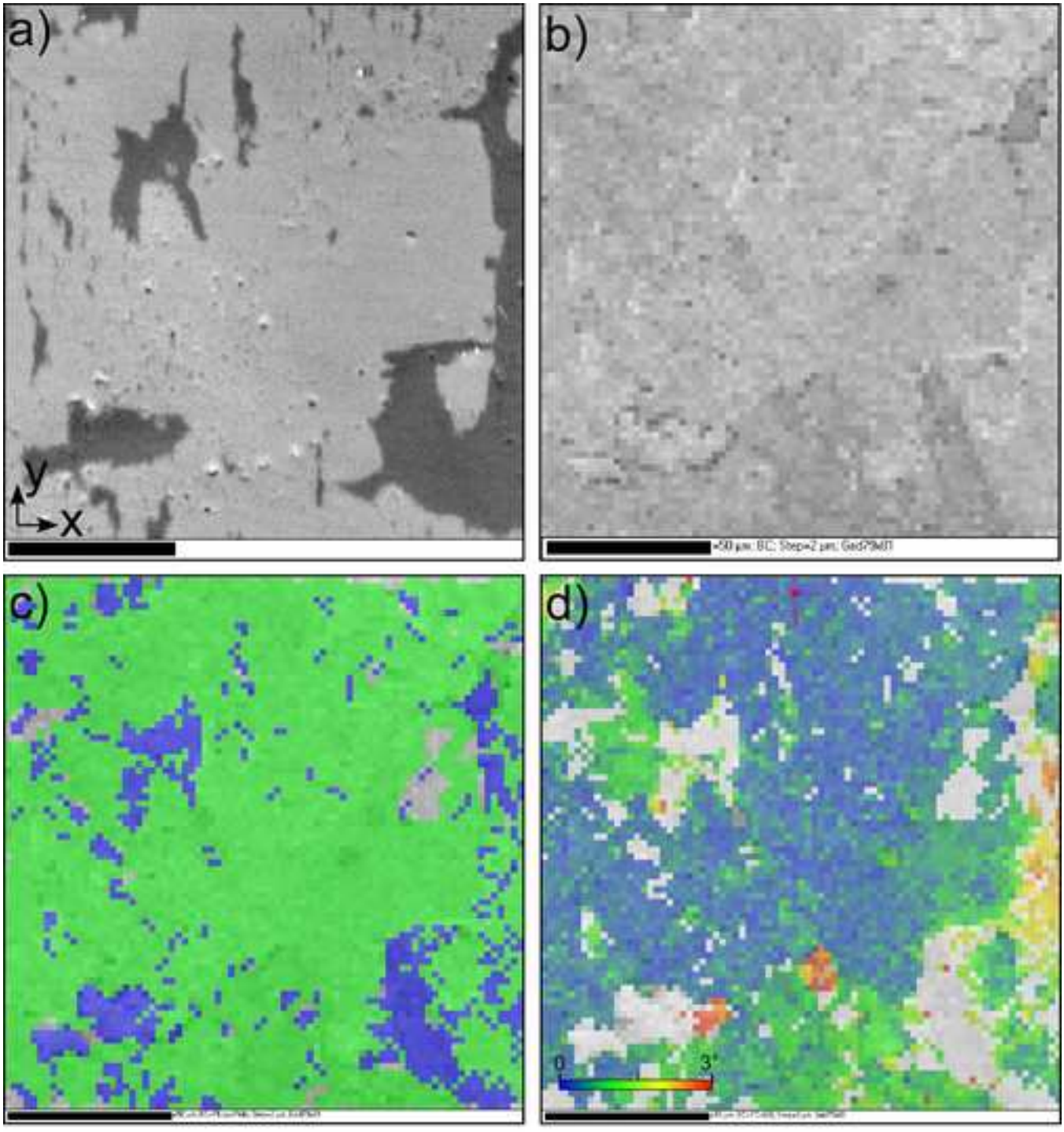

Figure 5

Figure 6

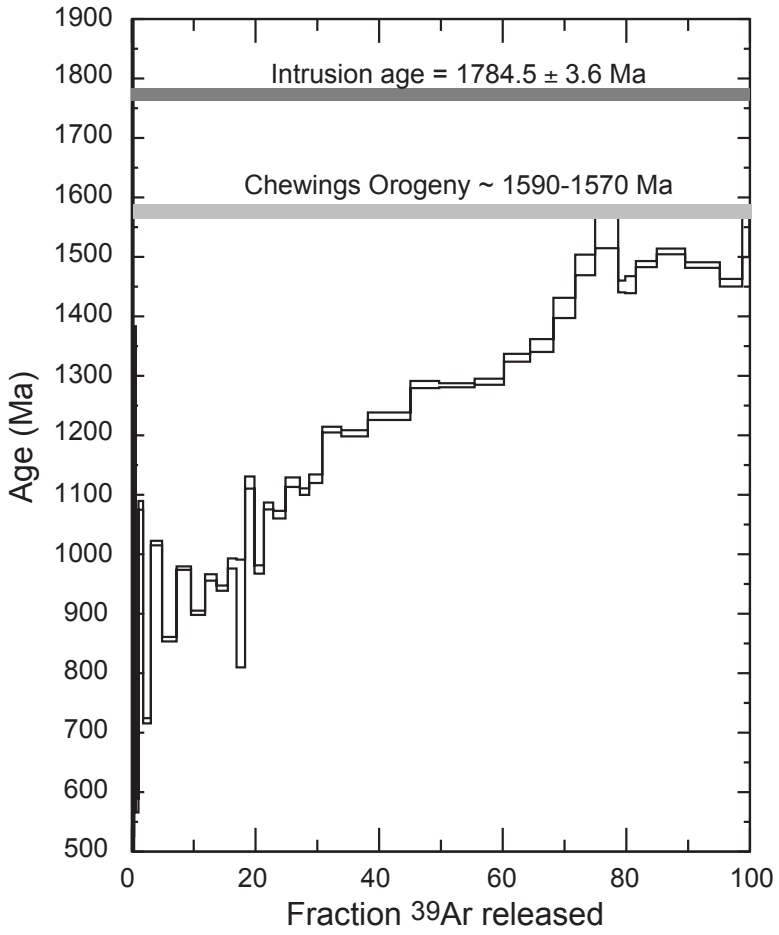

Figure 6

Figure 7

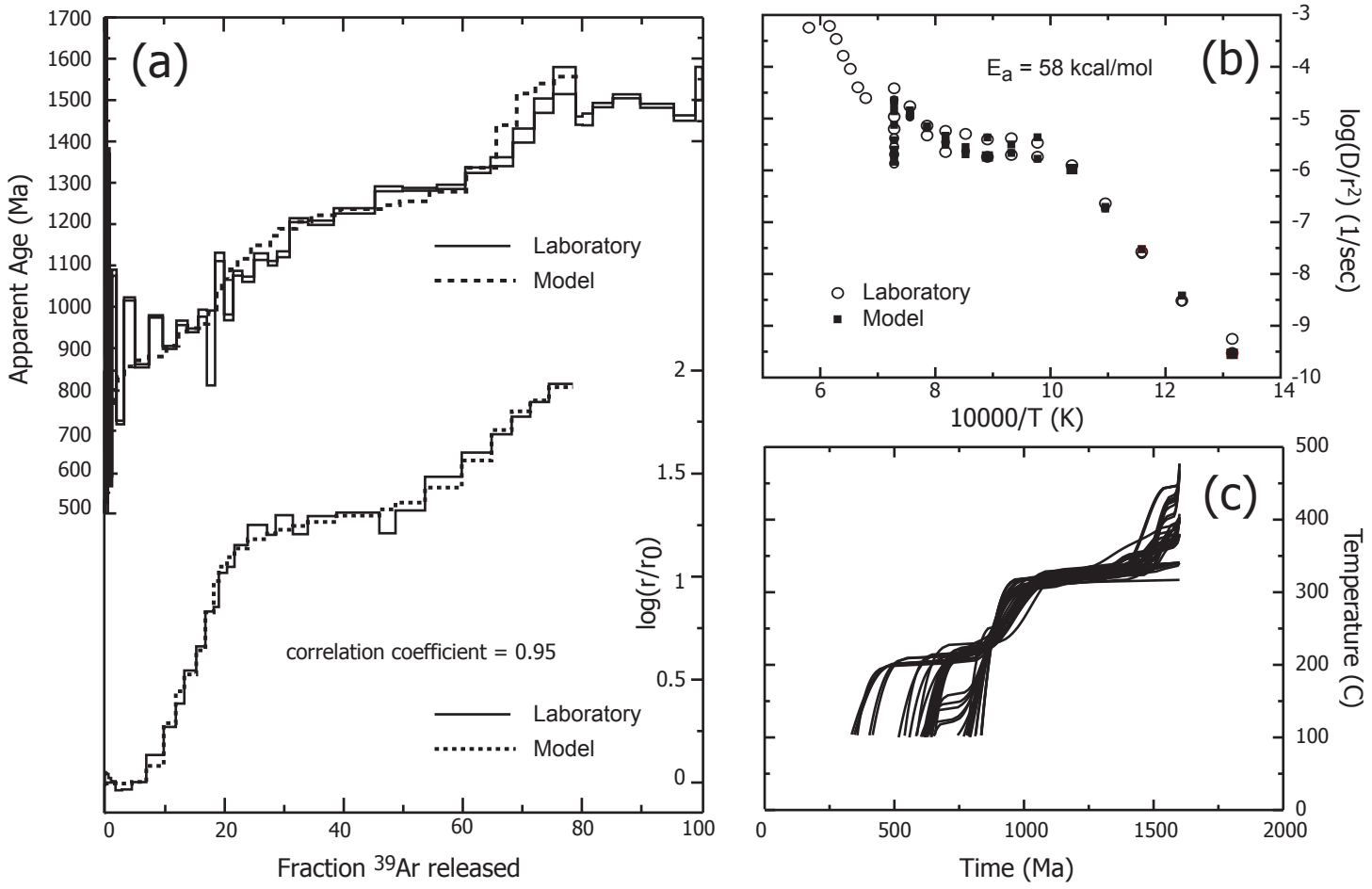

Figure 7

Figure 8

Click here to download high resolution image

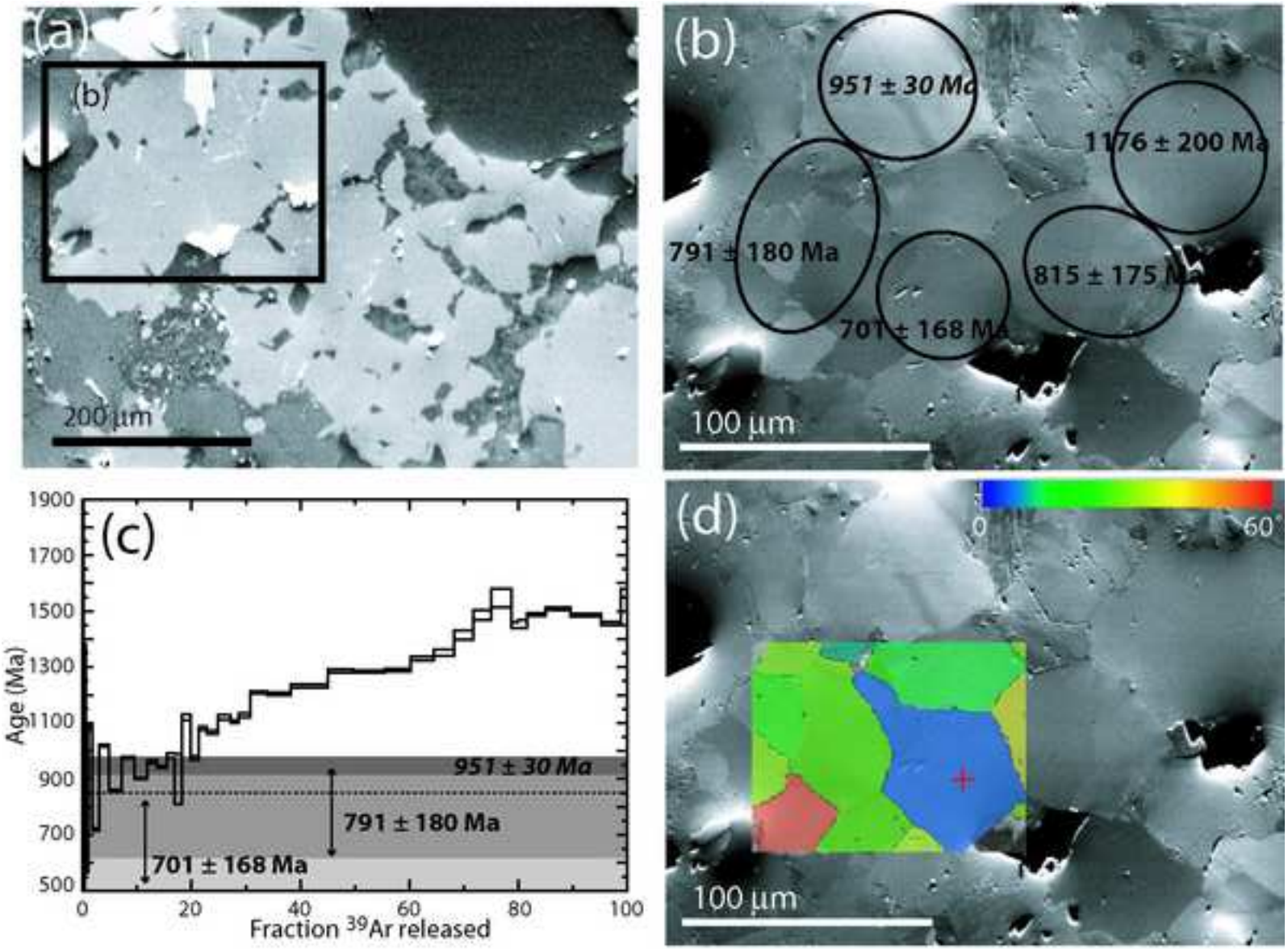

Figure 8

Figure 9

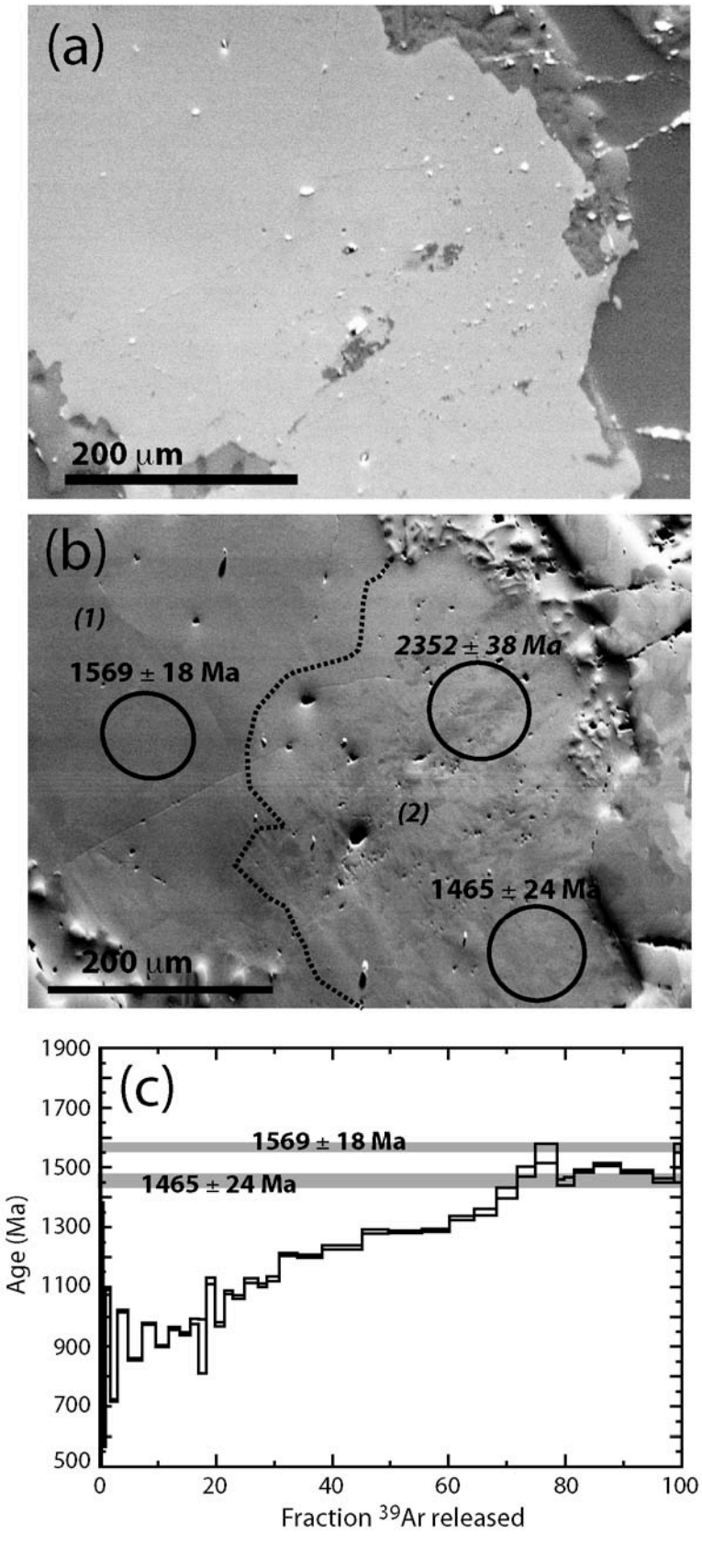

Figure 9